Reconstruction of Coronary Arteries from a Single Rotational X-Ray Projection Sequence

Christophe Blondel, Grégoire Malandain, Régis Vaillant, Nicholas Ayache

HAL Id: inria-00614993
https://hal.inria.fr/inria-00614993

Submitted on 17 Aug 2011

Reconstruction of Coronary Arteries from a Single Rotational X-Ray Projection Sequence

Christophe Blondel, Grégoire Malandain, Régis Vaillant and Nicholas Ayache

Abstract— **Cardiovascular diseases remain the primary cause of death in developed countries. In most cases, exploration of possibly underlying coronary artery pathologies is performed using X-ray coronary angiography. Current clinical routine in coronary angiography is directly conducted in 2-D projection images from several static viewing angles. However, for diagnosis and treatment purposes, coronary artery reconstruction is highly suitable. The purpose of this study is to provide physicians with a 3-D model of coronary arteries, *e.g.* for absolute three-dimensional measures for lesion assessment, instead of direct projective measures deduced from the images, which are highly dependent on the viewing angle. In this article, we propose a novel method to reconstruct coronary arteries from one single rotational X-ray projection sequence. As a side result, we also obtain an estimation of the coronary artery motion. Our method consists of 3 main consecutive steps: (1) 3-D reconstruction of coronary artery centerlines, including respiratory motion compensation, (2) coronary artery 4-D motion computation, and (3) 3-D tomographic reconstruction of coronary arteries, involving compensation for respiratory and cardiac motions. We present some experiments on clinical datasets, and the feasibility of a true 3-D Quantitative Coronary Analysis is demonstrated.**

Index Terms— **Angiocardiography, Coronarography, Image Motion Analysis, Image Reconstruction, Tomography**

I. INTRODUCTION

According to the World Health Organization [1, page 48], coronary heart disease is the major cause of death worldwide. In particular, coronary artery lesions are involved in most cases of heart failure and are thus the subject of medical imaging examinations when a pathology is suspected.

Currently, clinical routine relies on direct analysis of X-ray coronary angiographies acquired from several static acquisitions from distinct viewing angles. It thus produces 2-D measures (*e.g.* QCA – Quantitative Coronary Analysis) which suffer from well known viewing angle dependence, magnification factor, and superimposition effects. However, to achieve adequate therapeutic orientation, 3-D measures such as absolute vessel cross-sectional area would be of interest as they can be used to specify diameter and length of angioplasty balloons or stents to be used. In this context, three-dimensional reconstruction of coronary arteries would be of great clinical and diagnostic interest as it would provide physicians with 3-D absolute measures. Our purpose is thus to obtain tomographic reconstructions of coronary arteries, in a CT-like manner, from the most widely available imaging modality for coronary artery examination, X-ray coronary angiography.

Such 3-D information may be obtained by biplane angiography, since this modality provides two (almost) synchronized projections of the coronary arteries [2]–[4], or by selecting two views from two single-plane angiograms [5]. However, using only two projections is not sufficient to provide a precise measure of cross-section areas. Reconstructing the coronary arteries still remains a very challenging task, despite recent advances in medical imaging hardware and methodologies. In X-ray coronary angiography, the introduction of the digital flat panel [6] combined with a rotational acquisition mode [7] allowed for the proposal of new techniques in coronary artery modeling. The number of projections used for reconstruction can be increased by selecting the ones that correspond to the same cardiac time in a rotational acquisition, as in [8], [9], but most of the acquired images are discarded in such a procedure. By selecting projections close to a cardiac time, the number of used projections increases [10] but reconstruction artifacts may appear due to motion, and a significant number of acquired images are still discarded.

The main two difficulties that arise for the tomographic reconstruction of coronary arteries from angiograms are indeed the respiratory and cardiac motions that are visible in the X-ray projection sequence. In this article, we present a study that demonstrates the feasibility of the reconstruction of a 3-D image of the coronary arteries from *a single* rotational X-ray projection sequence, without requiring any additional measure (*e.g.* ECG).

Contrary to iterative methods that alternate between motion estimation and tomographic reconstruction (*e.g.* [11]), the proposed method is direct and consists of three major steps (see Fig. 1): (1) static 3-D reconstruction of coronary artery centerlines at one given cardiac phase, (2) estimation of 4-D motion from resulting set of 3-D lines, and (3) 3-D tomographic reconstruction of coronary arteries performed by integrating cardiac motion compensation. This last step is only sketched here, details can be found in [12].

The remainder of this article is organized as follows. In Section II, we describe the rotational acquisition protocol that was used and the datasets we were provided with. Sections III, IV, and V detail, respectively, the 3-D centerlines reconstruction (which is coupled with respiratory motion correction), the coronary artery motion estimation, and finally the tomographic reconstruction with motion compensation. Experiments on patient datasets are presented in Section VI, while the next Section VII discusses the proposed method and some potential clinical applications. Section VIII gives some perspectives.

Original Data

II–B. Preprocessing: data selection, pseudo ECG

Ref. 1   Ref. i   Ref. n

III. 3–D centerlines reconstruction

IV. 4–D motion estimation
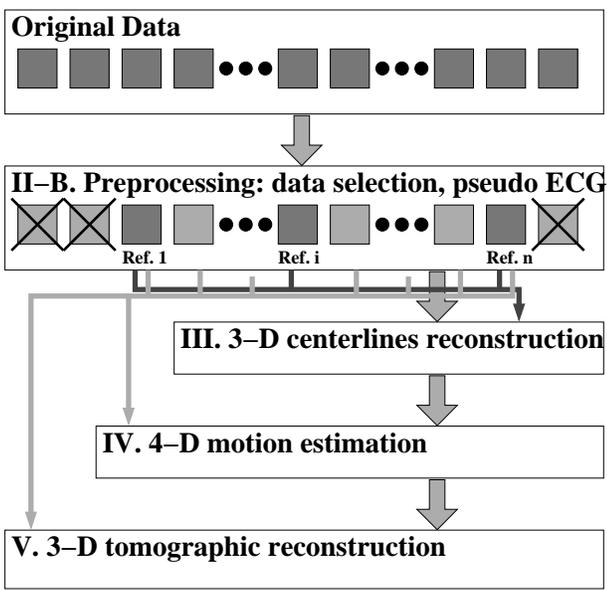
V. 3–D tomographic reconstruction

Fig. 1. Overview of the proposed method. The reference images (images that are synchronous w.r.t. the cardiac cycle) are identified in a pre-processing stage, and some data, at the extremities of the temporal sequence, are discarded. These reference images are used to reconstruct a static 3-D centerlines model at the reference time. This model and all the data allow the calculation of a 4-D deformation field that estimates the cyclic heart motion. This 4-D motion and all the data (from ref. 1 to ref. n) are finally used to provide the tomographic reconstruction of a 3-D image of the coronary arteries.

II. DATA AND PRE-PROCESSING

A. Data

Images were acquired on an Innova 2000 system, from General Electric HealthCare, which is equipped with a digital flat panel detector. The gantry performs a rotation while acquiring the images [13]. The gantry motion is characterized by constant SID (Source Intensifier Distance) value, constant CRA/CAU (Cranio/Caudal) angle value, and varying LAO/RAO (Left/Right Anterior Oblique) angle. Thus, the rotation occurs in patient axial plane, with maximum LAO/RAO angle amplitude of $200°$. Top rotation speed is $40°$ s^{-1}, leading from 3 to 5 seconds long acquisitions. Angiograph acquisition frame rate is 30 Hz. Thus, this protocol provides us with the imaging of 3 to 7 cardiac cycles. Images acquired at the same cardiac phase are approximately separated by a $30°$ angular shift, depending on patient heart rate.

For each patient, we have a single rotational sequence consisting of $\tilde{\mathcal{O}}$ images I_n with spatial resolution 768×768 pixels and pixel size of 0.2 mm. We resampled these images into a 512×512 lattice for computational purposes. In addition, a precalibration step allowed to estimate the geometrical acquisition parameters that are summarized in $\tilde{\mathcal{O}}$ projection matrix applications $\mathbf{M}_n : \mathbb{R}^3 \longrightarrow \mathbb{R}^2$, the matrix $\mathbf{M}_n$ being associated to image I_n.

B. Preprocessing

A prerequisite for our method is the identification of a pseudo-cardiac time (or observed cardiac phase) for all images in the sequence. This information is computed solely from the image sequence information, without any external measures such as ECG signal. The basic idea is the following: along the cardiac cycle, systole is characterized by myocardium contraction and a global top-to-bottom motion of the coronary tree in the axial direction, while diastole is characterized by myocardium relaxation and a global bottom-to-top motion of the coronary tree in the axial direction. In addition to the cardiac motion, the coronary arteries are also subject to the respiratory motion that consists mainly in a vertical translation in the axial direction, but of much lower frequency than the cardiac one. We then assumed that the high frequency part of the global vertical motion of coronary arteries in the image sequence is directly related to the cardiac phase.

To identify the vertical component of motion in the image sequence, we first compute for all images $I_n(x, y)$ the vector of horizontal line integrals $H_n(y) = \sum_x \bar{I}_n(x, y)$ of an associated local contrast image $\bar{I}_n(x, y)$ (obtained by applying a morphological top-hat operator [14] on the initial image I_n) over the horizontal coordinate. The vertical motion between two successive frames is estimated by identifying the shift along the vertical axis that minimizes the sum of squared differences between the corresponding H_n. The process is carried out over the complete sequence and leads to a nearly periodic signal over time, whose high frequency characterizes the heart beat. Quasi synchronous images can be easily identified by either selecting image indices at local maxima of the integral signal, located at end-diastole, or selecting image indices at local minima of the integral signal, located at end-systole [41]. In practice, quasi synchronous images acquired at end-diastole are preferred because they correspond to the most relaxed and stable state along heart motion, and consequently reduces superimpositions and potential asynchronism. The selected quasi synchronous images, which correspond to the same cardiac phase, are called *reference images*. The set of reference images will be denoted by $\mathcal{R}$ and its cardinal by $\tilde{\mathcal{R}}$.

Using reference image indices, we assign to each frame a *normalized time* that encodes the observed cardiac phase, relatively to cardiac phase in reference images. Normalized times belong to the $[0, 1[$ interval. The computation scheme is the following: two successive reference images are respectively assigned to normalized time $t = 0$ and normalized time $t = 1$, then normalized times of intermediate images are given by linear interpolation.

Time normalization is adapted to cardiac period changes during the acquisition, which is often the case, as contrast agent injection usually accelerates heart motion. Indeed, we do not assume that the number of acquired images between two references times is fixed for a given sequence. However, images before the first and after the last reference images can not be assigned a normalized time. In the following, we discard these images from the sequence to only consider the $\tilde{\mathcal{N}}$ images, $\tilde{\mathcal{N}} \leq \tilde{\mathcal{O}}$, between the first and last references images. The normalized time of image I_n is denoted t_n.

III. 3-D CENTERLINES RECONSTRUCTION

The first stage of our method is the reconstruction of 3-D centerlines from the reference images, corresponding to
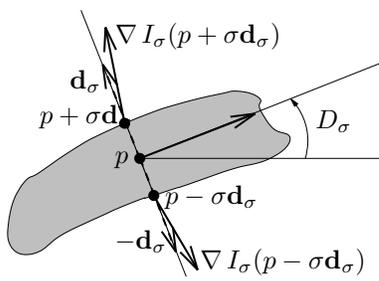
Fig. 2. Filter response computation scheme. Filter response at pixel p is computed by calculating an edge response on both sides of the potential rectilinear structure, at distance σ from pixel p in direction $\mathbf{d}_\sigma$ orthogonal to the structure direction D_σ.

normalized time $t = 0$. These images are selected from one single sequence and acquired at the same cardiac phase but from distinct viewing angles. Thus, they are supposed to be uncorrupted by cardiac motion, but are subject to respiratory motion. The extraction of the coronary artery centerline in 2-D images and their 3-D reconstruction, including the respiratory motion compensation, is detailed below.

A. Vessel enhancement

Our first prerequisite is to enhance the vessels in the angiograms. We used the approach first proposed in [15], [16] and extended in [17]. It relies on a multiscale Hessian-based filtering that enhances curvilinear structures.

For a given scale σ, an original image I is first convoluted with a 2-D Gaussian G_σ with standard deviation σ. The convoluted image is denoted by $I_\sigma = I * G_\sigma$. The Hessian matrix of the convoluted image is computed by:

$$\mathbf{H}I_\sigma = \begin{pmatrix} \frac{\partial^2 I_\sigma}{\partial x^2} & \frac{\partial^2 I_\sigma}{\partial y \partial x} \\ \frac{\partial^2 I_\sigma}{\partial x \partial y} & \frac{\partial^2 I_\sigma}{\partial y^2} \end{pmatrix} \quad (1)$$

where the second derivatives of I_σ are calculated by convoluting I with the corresponding second derivatives of G_σ. The eigenvalues and eigenvectors of the Hessian allow to characterize the local structures [18]. It follows that the direction D_σ of a potential locally rectilinear structure, *i.e.* a vessel, can be estimated by $\tan(2 D_\sigma) = 2 \frac{\partial^2 I_\sigma}{\partial x \partial y} / \left(\frac{\partial^2 I_\sigma}{\partial x^2} - \frac{\partial^2 I_\sigma}{\partial y^2} \right)$.

Let $\mathbf{d}_\sigma$ be an unitary vector orthogonal to direction D_σ. A vessel point should exhibit strong edge information (the vessel borders) at some distance in both directions $\mathbf{d}_\sigma$ and $-\mathbf{d}_\sigma$. We evaluate this edge information as the derivative of I_σ with respect to $\mathbf{d}_\sigma$ at a distance σ, and we end up with a filter designed for rectilinear structures:

$$R_\sigma(p) = \min \{\nabla I_\sigma(p+\sigma \mathbf{d}_\sigma).\mathbf{d}_\sigma, -\nabla I_\sigma(p-\sigma \mathbf{d}_\sigma).\mathbf{d}_\sigma\}. \quad (2)$$

Figure 2 shows an illustration of the filter response computation scheme. This filter enhances rectilinear structures with width close to scale σ. Moreover, it also has maximum response at vessel center. Since the observed vessels have highly varying sizes, the previous computation is extended to multiple scales and conducted for a set of scales Σ, adapted for smallest to largest vessels. In pixels length unit, for 512^2 spatial resolution images, we use $\Sigma = \{1, 2, 3, 4, 5, 6\}$. At each point p, the best scale $\sigma^\star(p)$ is selected according to the maximum filter response: $\sigma^\star(p) = \arg \max_{\sigma \in \Sigma} R_\sigma(p)$.

To compare and normalize the filter responses across scales, the concept of γ-derivatives was used [17], [19]. The direction and the response associated with the best local scale are collected into a multiscale direction $D^\star$ and a multiscale filter response map $R^\star$. This multiscale filter response $R^\star$ can be considered as a likelihood for pixels to belong to the projected centerline of a coronary artery.

B. 2-D centerlines extraction

From the above computed multiscale responses, we now build a set of 2-D curves that represent the coronary artery centerlines. This will be done in three steps: subpixel local directional maxima computation, hysteresis thresholding of local directional maxima, and points linking.

1) Subpixel local directional maxima extraction: $R^\star$ exhibits higher intensities in the center of a rectilinear structure than in the vicinity of its borders. A pixel p is then likely to belong to the vessel centerline if $R^\star$ is maximal at p along a direction orthogonal to the vessel. Such a direction is given by $\mathbf{d}_{\sigma^\star}(p)$, so pixel p is a local directional maximum if the following conditions hold: $R^\star(p) > R^\star(p + \mathbf{d}_{\sigma^\star})$ and $R^\star(p) > R^\star(p - \mathbf{d}_{\sigma^\star})$.

A subpixel estimation of the detected local maxima is achieved by fitting a quadric on points $(p - \mathbf{d}_{\sigma^\star}, R^\star(p - \mathbf{d}_{\sigma^\star}))$, $(p, R^\star(p))$, and $(p + \mathbf{d}_{\sigma^\star}, R^\star(p + \mathbf{d}_{\sigma^\star}))$. After some calculations, it turns out that this subpixel maximum $\hat{p}$ is given by

$$\hat{p} = p + \frac{R^\star(p - \mathbf{d}_{\sigma^\star}) - R^\star(p + \mathbf{d}_{\sigma^\star})}{2(R^\star(p + \mathbf{d}_{\sigma^\star}) + R^\star(p - \mathbf{d}_{\sigma^\star}) - 2R^\star(p))} \mathbf{d}_{\sigma^\star}. \quad (3)$$

The extracted set of points contains most of the vascular but also many non vascular structures that have to be excluded.

2) Hysteresis thresholding: most of the irrelevant local directional maxima that do not correspond to vascular structures are characterized by a low multiscale filter response and the small size of the connected components they belong to. Hysteresis thresholding is suited to discard them since it offers the possibility to retain only the elements that match both an intensity criterion and a criterion of size of the connected components. Hysteresis thresholding requires both a high and a low thresholds. We compute these thresholds as quantiles of the cumulated histogram of the multiscale filter response maps over the complete sequence. The low threshold is set to a typical value of the multiscale filter response on vessels, while the high threshold is set to a typical value of the multiscale filter response on vessel centerlines. These quantiles can be related to relative area respectively occupied by vessels and vessel centerlines in the images. From our experiments, we chose the 90th percentile for the low threshold and the 98th percentile for the high threshold. In addition, hysteresis thresholding allows to retain only sufficiently large connected components. The minimal connected component size was set to 5 pixels.
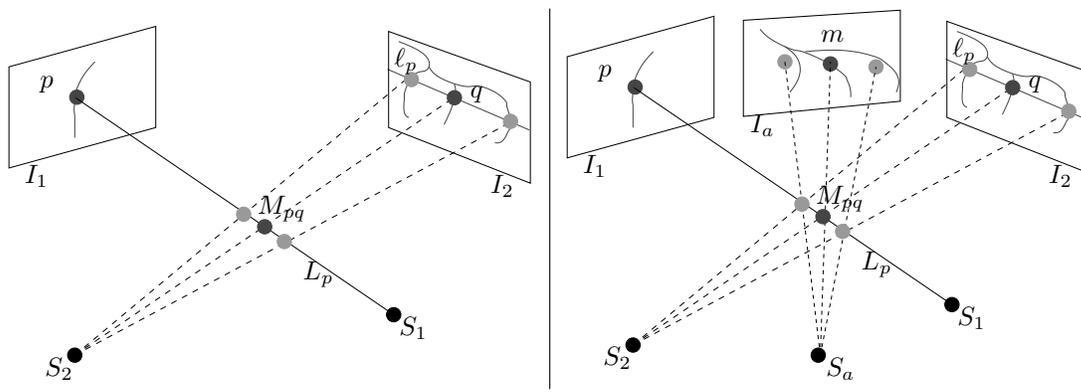
Fig. 3. Epipolar constraint. The 3D point that projects at p in image I_1 is located on the 3D line L_p (that joins p to S_1). Consequently, its projection in image I_2 is located on the projection ℓ_p of the line L_p. With two images (left), there are many possible 3D points as intersections of ℓ_p with vessels in I_2. However, only one of them projects on a vessel in the additional image I_a (right). This allows to penalize spurious reconstructed 3D points.

3) Points linking: local directional maxima have been extracted point-wise, but vessels projected in images have a connected structure. We recover this structure by linking points that belong to the same component using the method described in [20]. We denote by $\mathcal{C}_I$ the set of the 2-D connected centerlines extracted from image I.

C. Multi-ocular matching

Building correspondences between the centerlines of two reference images, I_1 and I_2, that are from the same cardiac phase but acquired from two distinct viewing angles, enables the three-dimensional reconstruction of the coronary artery centerlines by applying triangulation and epipolar constraints.

Most of the proposed approaches for 3-D reconstruction of coronary artery centerlines rely on only two angiographic views [21], typically obtained by biplane angiography. The rotational acquisition allows to get between 3 and 7 reference frames, depending on gantry rotation speed and on patient heart rate. We propose to use all the available images to perform a multi-ocular matching of the extracted centerlines in reference images, as basically described in [22]. This is achieved by optimizing a matching criterion detailed below.

1) Asymmetric matching: let us first consider the asymmetric problem of matching a set of linked points, denoted by $C = (p_1, \ldots, p_N) \in \mathcal{C}_{I_1}$, in a first image I_1, with the extracted centerline points in a second image I_2.

▷ Problem formulation: As illustrated by Figure 3, a point p in I_1 is the projection of a 3-D point M located in 3-D line L_p, joining source position S_1 to projection position p. The projection of the 3-D line L_p in I_2, denoted ℓ_p, must contain the projection q of M in I_2: this is the *epipolar constraint*.

Unfortunately, the epipolar constraint does not generally yield a single match in I_2 for each $p \in I_1$. Indeed, in most cases, line ℓ_p intersects more that one centerline in I_2, resulting in a set of matching candidates in I_2 (see Figure 3, left). Our experiments shows an average of 5 matching candidates per point. Let $\mathcal{Q}_i$ denote the set of matching candidates in I_2 for point p_i in I_1. Building the correspondences for a set of linked points

$(p_1, \ldots, p_N)$ of I_1 consists then in choosing a set of points $\{q_1, \ldots, q_N\} \in \mathcal{Q}_1 \times \cdots \times \mathcal{Q}_N$.

To compare different matching configuration, we now design a criterion to measure the quality of a given matching hypothesis $(p_i, q_i)_{i=1\ldots N}$. This quality measure is composed of an external energy term, involving reference images information, and an internal energy term, favoring intrinsically coherent matching configurations, that are both detailed hereafter.

▷ External energy term: To disambiguate between the matching candidates, the reference images other than I_1 and I_2 are used. This additional information is indeed useful: among the several matching candidates given by the epipolar constraint, only one will be coherent with the additional views in most cases. As shown on the right hand side of Figure 3, to each epipolar candidate corresponds a 3-D point using reconstruction by triangulation, whose projection in additional images is on a vessel only for the correct correspondence.

A numerical criterion that reflects the relevance of a reconstructed 3-D point is the value of the multiscale filter response of its projection in the additional views. Let $I_a \in \mathcal{R} \setminus \{I_1, I_2\}$ be such an additional view (from the same cardiac phase than I_1 and I_2 by the definition of $\mathcal{R}$). To any given matching pair (p, q) corresponds a 3-D reconstructed point M_{pq}, whose projection in additional image I_a is $m = \mathbf{M}_a M_{pq}$. We recall that $R_a^\star$ is the multiscale filter response map associated to the additional image of index a. The external energy term measuring matching pair (p, q) quality is defined by:

$$AM_{\text{Ext}}(p, q) = \frac{1}{\tilde{\mathcal{R}} - 2} \sum_{I_a \in \mathcal{R} \setminus \{I_1, I_2\}} R_a^\star(\mathbf{M}_a M_{pq}) \quad (4)$$

where $\tilde{\mathcal{R}}$ stands for the number of reference images. This criterion reaches high values for matching pairs that are coherent with additional reference images.

▷ Internal energy term: the above criterion is convenient for points, but does not take into account the intrinsic linked structure of vessel centerlines. Indeed, a linked set of points in image I_1, that represents a detected centerline, is more likely to project as a single connected component
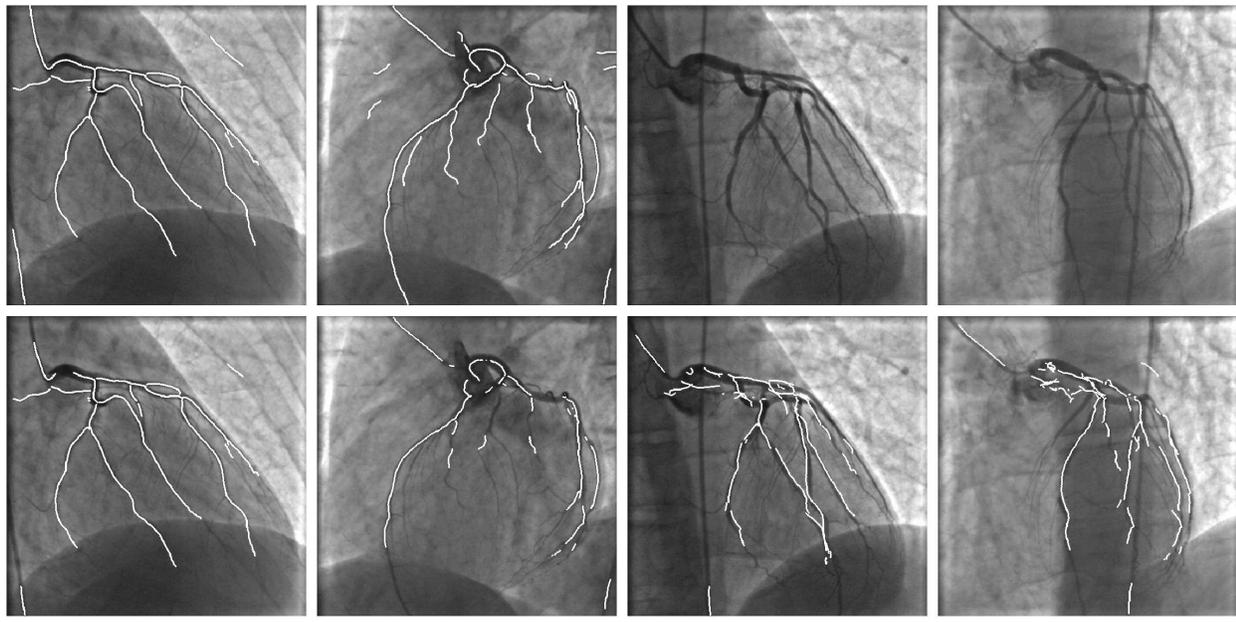
Fig. 4. Results of the dynamic programming based matching process. Centerlines in the first reference image are matched with centerlines in the second reference image (images in top row) according to the information contained in the two additional views (last images in top row). Projection of the 3-D reconstructed points is presented in all reference images (bottom row).

in other reference images than as disconnected pieces. Exceptions may occur in case of superimposition or defective centerlines extraction. This constraint is called *geometrical coherence*.

Let (p_1, q_1) and (p_2, q_2) denote two matching pairs, where p_2 follows p_1 in a set of linked points in the extracted centerline in I_1. We define the penalty for two successive matching point pairs as a function of the distance $\|q_1 q_2\|$:

$$AM_{\text{Int}}((p_1, q_1), (p_2, q_2)) = \rho(\|q_1 q_2\|) \qquad (5)$$

$$\text{with } \rho(d) = \begin{cases} 0, & \text{if} \quad d \leq d_l \\ \frac{d - d_l}{d_h - d_l}, & \text{if} \quad d_l < d < d_h \\ 1, & \text{else} \end{cases} . \qquad (6)$$

Thresholds d_l and d_h are chosen such that matched points whose distance is below d_l are not penalized, and such that the ones whose distance is above d_h are not over-penalized since they may indicate a discontinuity in the matching points sequence. Typically, $d_l = 2$ pixels and $d_h = 50$ pixels for 512^2 images.

▷ Matching criterion: Finally, the criterion measuring the quality of a matching configuration $(p_i, q_i)_{i=1...N}$ is chosen to be the weighted sum of the external energy term for all points pairs and of the internal energy term for all successive points pairs:

$$AM\left((p_i, q_i)_{i=1...N}\right) = - \sum_{i=1...N} AM_{\text{Ext}}(p_i, q_i)$$
$$+ \alpha \sum_{i=1...N-1} AM_{\text{Int}}((p_i, q_i), (p_{i+1}, q_{i+1})). \qquad (7)$$

The optimal set of correspondences, $\{\hat{q}_1, \ldots, \hat{q}_N\} = \arg\min AM((p_i, q_i)_{i=1...N})$, is computed by a dynamic

programming based approach [23], which enables to find the global optimum in predictable time and low computational complexity. We denote by $\hat{AM}(C, \mathcal{C}_{I_2}) = \hat{AM}((p_1, \ldots, p_N), \mathcal{C}_{I_2}) = AM((p_i, \hat{q}_i))$ the minimal value of the asymmetric matching criterion.

This optimization is repeated for all sets of linked points of image I_1. Figure 4 shows an example of results provided by matching process. The sum of the above matching criterion over all the sets of linked points in I_1 is assumed to be a quality measure of the 3-D reconstruction of all vessel centerlines: it is defined by $\sum_{C \in \mathcal{C}_{I_1}} \hat{AM}(C, \mathcal{C}_{I_2})$ and we call it the *global asymmetric matching criterion*. Note that this criterion depends on the projection matrices $\mathbf{M}$ (see Eq. (4)).

2) Matching symmetrization: the above described reconstruction method is intrinsically asymmetric. Centerlines in image I_1 are matched with centerlines in image I_2 according to the remaining images, and the result depends on the choice of both images I_1 and I_2 which is undesirable.

A *symmetric* reconstruction is then achieved by considering all ordered pairs of images among the reference images. With our notations, we end up considering $\tilde{\mathcal{R}}(\tilde{\mathcal{R}} - 1)$ pairs of images. This yields a number of 3-D reconstructed centerlines. The ones that are supposed to represent the same 3-D vessel may be slightly shifted from each other, mainly because of the respiratory motion, but also of an imperfect synchronization of reference images and of geometrical reconstruction errors.

Figure 5 shows the result of this symmetric reconstruction. The *global matching criterion* after symmetrization is merely given by the sum of all *global asymmetric matching criteria* over all ordered pairs of reference images, and is defined by

$$\sum_{I_1 \in \mathcal{R}} \sum_{I_2 \in \mathcal{R} \setminus \{I_1\}} \sum_{C \in \mathcal{C}_{I_1}} \hat{AM}(C, \mathcal{C}_{I_2}). \qquad (8)$$
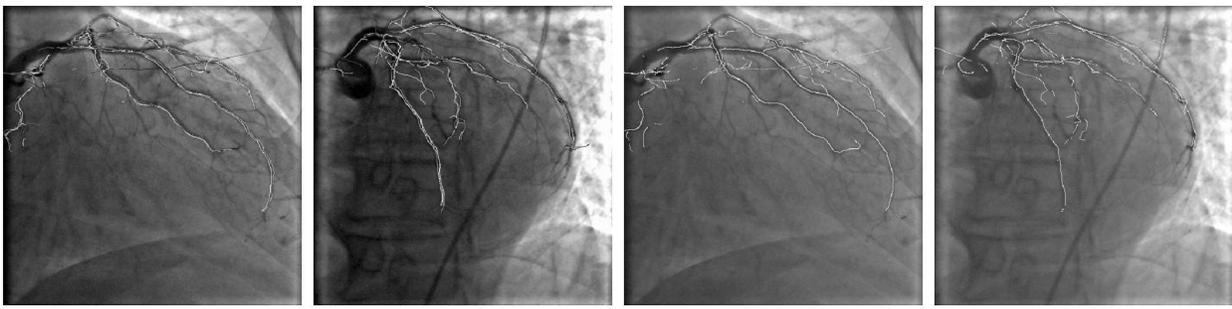
Fig. 5. Left, symmetric reconstruction: projection in two reference images of the centerlines reconstructed by considering all the ordered pairs of four reference images (a different greytone is associated with each asymmetric reconstruction), 3-D centerlines reconstructions appear redundant and slightly shifted. Right, fusion of the redundant 3-D reconstructed centerlines sets presented at left: the reconstructed centerlines after applying the fusion process are projected in two reference images. A *geometrically average* reconstruction has been built.

a) Respiratory motion compensation: as shown in [24]–[27], the respiratory motion effect on the myocardium, and thus on the coronary artery position, can be approximated by a 3-D translation, mainly in the axial direction. From the acquisition point of view, it corresponds to a translation of the images in their acquisition plane, that can be encoded in the calibration parameters, *i.e.* in the $\mathbf{M}_n$ matrices. Indeed, as demonstrated in [28], the global matching criterion reaches its minimum for optimal calibration parameters. We thus consider optimizing the global matching criterion with respect to the cameras translation in their acquisition plane, *i.e.*

$$\left\{\hat{\mathbf{M}}_i\right\}_{i/I_i \in \mathcal{R}} = \arg\min_{\mathbf{M}_i} \sum_{I_1 \in \mathcal{R}} \sum_{I_2 \in \mathcal{R}\setminus\{I_1\}} \sum_{(p_1,\ldots,p_N)\in\mathcal{C}_{I_1}}$$

$$\min_{\{q_j\}\subset\mathcal{C}_{I_2}} \left[-\sum_{j=1\ldots N} \frac{1}{\tilde{\mathcal{R}}-2} \sum_{I_a\in\mathcal{R}\setminus\{I_1,I_2\}} R_a^\star\left(\mathbf{M}_a M_{p_j q_j}\right) \right.$$

$$\left. +\alpha \sum_{j=1\ldots N-1} \rho(\|q_j q_{j+1}\|) \right] \qquad (9)$$

in order to estimate the respiratory motion. As a side result, we also obtain the 3-D reconstructed centerlines for the optimal projection matrices.

To optimize the global matching criterion, we use a FSQP optimization method implementation [29], [30]. It results in a translational correction in acquisition plane for reference images, reflecting respiratory motion effect. We propagate this information to other than reference images by linearly interpolating corrections that were found for the two surrounding reference frames.

3) Reconstruction fusion: the respiratory motion compensation improved the reconstruction of 3-D centerlines, particularly by reducing the slight shift observed between asymmetric reconstructions, but is not sufficient to yield a *perfect* superimposition of the 3-D centerlines obtained from the different asymmetric reconstruction. Keeping multiple reconstructions of the same 3-D vessels may bias the forthcoming 4-D motion estimation since it introduces spatial imprecision. Consequently, we fuse the distinct reconstructed centerlines sets in a single set where previously redundant points appear only once. We also store redundancy information, as it is a

useful indicator for confidence in reconstructed points.

The fusion relies on a threshold representing the maximum shift distance allowed for redundant points. We set it to 5 millimeters which is an approximate value for largest observable coronary artery diameter. Two 3-D centerline sets are fused in a geometrical manner: for each point in the first set, we find the closest point in the second set, if their distance is smaller than a distance threshold, then points are considered redundant and are replaced by their barycenter, else the closest point is added as a new point. Iterating this process for all 3-D reconstructed centerline sets leads to a fused 3-D centerline reconstruction. Figure 5 illustrates the effect of fusion on redundant 3-D reconstructed centerline sets.

Additionally, redundancy of fused points is given by the number of points that contributed to the fused point position. In practice, we build an application $\Lambda : \mathcal{M} \longrightarrow \mathbb{R}$, which associates the number of contributions $\Lambda(M)$ to any point M in the fused 3-D centerlines set $\mathcal{M}$. $\Lambda(M)$ can be interpreted as the confidence value for the 3-D reconstructed point M.

At the end of this first stage, we have 3-D reconstructed centerlines, including confidence indices, that have been corrected from respiratory motion effect. This reconstruction was obtained from a few images from the same cardiac phase.

IV. 4-D MOTION COMPUTATION

From above computations, a 3-D reconstruction of the coronary artery centerlines at the cardiac reference time is obtained, as well as the respiratory motion compensation for all the rotational sequence images. This 3-D model will now be used to estimate the cardiac motion.

Contrary to 3-D motion approaches usually involved in the biplane case [2], [31], that estimate a 3-D motion from time to time, we use all frames simultaneously, independently from the cardiac phase at which they were acquired, to estimate a global motion, parameterized over space and time, hence called 4-D motion.

Contrary to Chen's approach [32] that requires a 3-D reconstruction at each cardiac cycle and the explicit establishment of correspondences between 3-D reconstructions to compute the 4-D motion, only one single 3-D reconstruction (at the reference cardiac cycle) is needed here, and the 4-D motion is inferred from image-based measures.

A. Motion parameterization

To choose a motion parameterization, we recall some features of coronary artery motion: spatial and temporal smoothness and semi-local spatial and temporal influence.

These characteristics led us to choose a parameterization based on B-hypersolid, which is a 4-D tensor product of 1-D B-splines $B()$ [33]. This parameterization is a generalization of 3-D B-solids proposed in [34].

Extremal space coordinates are computed from the bounding box of the 3-D centerlines set $\mathcal{M}$. The spatial support was sampled using control points spaced 2 centimeters apart, leading to typically 10 control points along each spatial dimension. Time extremal values were given by the interval $[0, 1[$. This interval was sampled using 10 control points. In practice, we used cubic B-splines, providing a sufficient number of degrees of freedom. Knots vectors on space coordinates were chosen open uniform. This allowed one of the B-spline basis functions to be non null on the spatial bounds of the motion, and thus the motion may be non null on the spatial bounds of the motion support. On the opposite, knots vector in time coordinate was chosen uniform. This properties enforces that all B-spline basis functions to be null on the temporal bounds, and thus that the motion was constrained to be null at equivalent reference times $t = 0$ and $t = 1$.

Sets $\mathcal{I}$, $\mathcal{J}$, and $\mathcal{K}$ respectively discretize x, y, and z space coordinates, set $\mathcal{L}$ discretizes time coordinate. Their respective cardinals are $\tilde{\mathcal{I}}$, $\tilde{\mathcal{J}}$, $\tilde{\mathcal{K}}$, and $\tilde{\mathcal{L}}$. Under a B-hypersolid motion $\Phi : \mathbb{R}^p \times \mathbb{R}^3 \times \mathbb{R} \longrightarrow \mathbb{R}^3$, parameterized by vector $\mathbf{p} \in \mathbb{R}^p$ (the knot points coordinates), the position of point $M = (x, y, z)$ after the application of the displacement, evaluated at normalized time t, is given by:

$$\Phi(\mathbf{p}, M, t) = M + \sum_{i,j,k,l} B_i(x) B_j(y) B_k(z) B_l(t) \mathbf{p}_{ijkl}$$

$$\text{with } \mathbf{p}_{ijkl} \in \mathbb{R}^3 \quad \forall i, j, k, l. \tag{10}$$

B. Motion optimization

Estimating the heart motion now boils down to finding the optimal parameter vector $\hat{\mathbf{p}}$ that will exhibit the best coherence with the 2-D displacements observed in images I_n. This is achieved through the optimization of a criterion that aims at quantitatively evaluating the coherence of a B-hypersolid motion $\Phi(\mathbf{p}, ., .)$ with the angiogram sequence, through an external energy term, and that penalizes degenerate motions, through a regularization term.

The multiscale filter response, $R_n^\star$, is used as the likelihood that a pixel belongs to an artery projection. Summing the values of these responses for the projected 3-D reconstructed points M under motion gives us the external energy term $\Psi : \mathbb{R}^p \longmapsto \mathbb{R}$ of the criterion:

$$\Psi(\mathbf{p}) = \frac{1}{\tilde{\mathcal{N}}\tilde{\Lambda}} \sum_{n \in \mathcal{N}} \sum_{M \in \mathcal{M}} \Lambda(M) R_n^\star \left(\hat{\mathbf{M}}_n \left(\Phi\left(\mathbf{p}, M, t_n\right) \right) \right)$$

$$\text{with} \quad \tilde{\Lambda} = \sum_{M \in \mathcal{M}} \Lambda(M). \tag{11}$$

Note that the multiscale filter response of projected point M is weighted by its reconstruction confidence $\Lambda(M)$.

Successive steps for the evaluation of external energy term of the criterion are then:

- motion application $\Phi : \mathbb{R}^p \times \mathbb{R}^3 \times \mathbb{R} \longmapsto \mathbb{R}^3$,
- projection application $\hat{\mathbf{M}}_n : \mathbb{R}^3 \longmapsto \mathbb{R}^2$,
- multiscale filter response value $R_n^\star : \mathbb{R}^2 \longmapsto \mathbb{R}$, and
- weighting by confidence index $\Lambda : \mathcal{M} \subset \mathbb{R}^3 \longrightarrow \mathbb{R}$.

To prevent degenerated optimal motions, we add three internal energy terms which penalize motions with large amplitude, motions with erratic spatial behavior, and motions with erratic temporal behavior.

To estimate the motion amplitude, we evaluate the normalized sum over the control points of the square norm of vectors $\mathbf{p}_{ijkl}$:

$$\Gamma_1(\mathbf{p}) = \frac{1}{\tilde{\mathcal{I}}\tilde{\mathcal{J}}\tilde{\mathcal{K}}\tilde{\mathcal{L}}} \sum_{i,j,k,l} \|\mathbf{p}_{ijkl}\|^2. \tag{12}$$

To estimate the motion smoothness, we evaluate the normalized sum over the control points of the square norm of the vector difference between $\mathbf{p}_{ijkl}$ and its spatial neighbors $\mathcal{V}_{\mathbb{R}^3}(\mathbf{p}_{ijkl})$ (in terms of 26-connectivity in 3-D) and its temporal neighbors $\mathcal{V}_T(\mathbf{p}_{ijkl})$ (in terms of 2-connectivity in 1D):

$$\Gamma_2(\mathbf{p}) = \frac{1}{\tilde{\mathcal{I}}\tilde{\mathcal{J}}\tilde{\mathcal{K}}\tilde{\mathcal{L}}} \sum_{i,j,k,l} \frac{1}{\tilde{\mathcal{V}}_{\mathbb{R}^3}(\mathbf{p}_{ijkl})} \sum_{\mathbf{p}_{i'j'k'l} \in \mathcal{V}_{\mathbb{R}^3}(\mathbf{p}_{ijkl})} \|\mathbf{p}_{ijkl} - \mathbf{p}_{i'j'k'l}\|^2 \tag{13}$$

$$\Gamma_3(\mathbf{p}) = \frac{1}{\tilde{\mathcal{I}}\tilde{\mathcal{J}}\tilde{\mathcal{K}}\tilde{\mathcal{L}}} \sum_{i,j,k,l} \frac{1}{\tilde{\mathcal{V}}_T(\mathbf{p}_{ijkl})} \sum_{\mathbf{p}_{ijkl'} \in \mathcal{V}_T(\mathbf{p}_{ijkl})} \|\mathbf{p}_{ijkl} - \mathbf{p}_{ijkl'}\|^2 \tag{14}$$

where $\tilde{\mathcal{V}}_{\mathbb{R}^3}(\mathbf{p}_{ijkl})$ and $\tilde{\mathcal{V}}_T(\mathbf{p}_{ijkl})$ are the respective cardinals of sets $\mathcal{V}_{\mathbb{R}^3}(\mathbf{p}_{ijkl})$ and $\mathcal{V}_T(\mathbf{p}_{ijkl})$.

The final criterion for 4-D motion optimization is:

$$\Upsilon(\mathbf{p}) = \Psi(\mathbf{p}) - \alpha_1 \Gamma_1(\mathbf{p}) - \alpha_2 \Gamma_2(\mathbf{p}) - \alpha_3 \Gamma_3(\mathbf{p}). \tag{15}$$

The knot vectors properties and discretization scheme lead to approximately 10 degrees of freedom along each coordinate, a degree of freedom being a three-dimensional vector. Thus, vector $\mathbf{p}$ typically has $30\,000$ components. Consequently, optimizing the criterion requires a method dedicated to very large scale nonlinear optimization problems. It can be noticed that the four terms of Υ can be analytically derived. For instance, the gradient of Ψ is given below:

$$\frac{\partial \Psi(\mathbf{p})}{\partial \mathbf{p}} = \frac{1}{\tilde{\mathcal{N}}\tilde{\Lambda}} \sum_{n,M} \Lambda(M) \frac{\partial R_n^\star}{\partial \mathbf{M}_n} \frac{\partial \hat{\mathbf{M}}_n}{\partial \Phi} \frac{\partial \Phi(\mathbf{p}, M, t_n)}{\partial \mathbf{p}} \tag{16}$$

As an optimization procedure, we thus chose the Polak-Ribière variant of the nonlinear conjugate gradient algorithm [35] and used the CONMIN implementation described in [36]. The initial motion is set to null ($\mathbf{p} = \mathbf{0}$). Optimization process leads to an optimal parameterization $\hat{\mathbf{p}}$ and associated optimal motion $\Phi(\hat{\mathbf{p}}, ., .) : \mathbb{R}^3 \times \mathbb{R} \longrightarrow \mathbb{R}^3$ that will thereafter simply be denoted by Φ. The motion $\Phi(., t) : \mathbb{R}^3 \longrightarrow \mathbb{R}^3$ for a given normalized time t is denoted Φ_t. Figure 6 presents the results for motion computation by comparing 3-D centerlines projection before and after 4-D motion application.
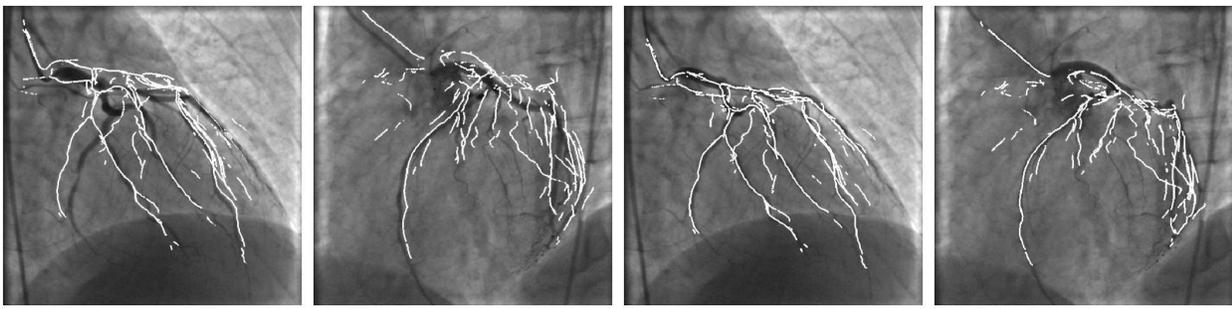
Fig. 6. Results for 4-D motion computation. Left: projection in two images (acquired at two distinct normalized times, all differing from the reference time) of the 3-D centerlines reconstruction before 4-D motion application. Right: projection in the same two images of the 3-D centerlines reconstruction after 4-D motion application. According to centerlines superimposition on vessels, 4-D motion has been correctly determined by the optimization process.

V. 3-D TOMOGRAPHIC RECONSTRUCTION

In our case, datasets differ from ideal tomographic conditions in two ways: data truncation for background structures that are located far from the gantry rotation center and coronary artery motion occurring during the acquisition.

A. Background removal

The angiograms include not only the structure of interest, *i.e.* the coronary vessels, but also background structures. Some of these structures are not visible in all the views because the field of view is smaller than the patient's torso. Consequently, they can potentially induce the so-called truncation artifacts during the reconstruction [37]. So, we apply a subtraction technique before the reconstruction in view of applying the reconstruction to projection data formed only by the arteries. A mask image is required to perform the subtraction and is obtained by processing the angiograms.

Thus, we have to produce virtual mask angiograms from original angiograms. This is done in four steps: binary vessel detection, virtual background image computation, virtual mask image computation, and virtual subtracted image computation.

The first step is done by applying an hysteresis thresholding to the multiscale filter response maps. The low and high thresholds are chosen equal to those used during centerline detection. To manage potential detection defects near the bifurcations or at distal parts of coronary arteries, this binary image is dilated using mathematical morphology [14]. The second step is achieved by applying a morphological closing to the original image, this leads to an approximation of the corresponding image, acquired without contrast agent injection. The third step is performed combining these two images in the following way: for any pixel, its virtual mask image value is given by the virtual mask image value, if the pixel belongs to a vessel according to the binary vessel detector image, or by the original image value, if the pixel does not belong to a vessel. This third image is a virtual mask of the original image. The last step is the logarithmic subtraction of the original image I_n and the virtual mask image to produce the virtually subtracted image J_n that will be actually used as tomographic data [41].

B. Motion compensated tomography

Classical tomographic reconstruction methods make the hypothesis that the observed object remains still during sinogram acquisition, which is of course not the case for coronary angiography. Many approaches propose to restraint the sinogram to the angiograms that were acquired at given cardiac phase [8], [9] or to phases that remain close to a reference phase [38]. This leads to few views tomographic reconstructions and often suffers from strong artifacts due to lack of data.

On the contrary, we use all available frames, homogeneously and independently from the cardiac phase they correspond to. In [11], the authors propose an iterative scheme alternating between motion estimation and tomographic reconstruction, in the context of CT. Here, we use a *single-pass* reconstruction method. We only give here a brief overview of the tomographic reconstruction, a complete and detailed description of the method can be found in [12].

The tomographic reconstruction is done by integrating the 4-D motion estimation into the tomographic projection operator matrix. Given a voxel set that discretizes the 3-D region of interest, the projection operator matrix coefficient $\mathbf{P}_{i,k}$ encodes the contribution of voxel v_k to pixel p_i in image n. The solid angle with origin the X-ray source S_n at frame n passing by pixel p_i edges is denoted Ω_{p_i}. In the static case, those contributions are estimated as the volume of the intersection between the voxel and the solid angle, *i.e.*:

$$\mathbf{P}_{i,k} = \text{volume } (\Omega_{p_i} \cap v_k) \qquad (17)$$

After a few calculations [12], the contribution in the dynamic case is obtained by: $\mathbf{P}_{i,k}^{\Phi} = \text{volume } (\Omega_{p_i} \cap \Phi_{t_n}(v_k))$.

We chose to neglect the relative volume variation effect, and to use a single contribution scheme (a voxel contributes to only one pixel per projection image J_n):

$$\mathbf{P}_{i,k}^{\Phi} = \begin{cases} \text{volume } (v_k) & \text{if } \Phi_{t_n}(c(v_k)) \in \Omega_{p_i} \\ 0 & \text{else} \end{cases} \qquad (18)$$

where $c(v_k)$ is the center of voxel v_k.

As the projection operator matrix $\mathbf{P}^{\Phi}$ has been corrected for cardiac motion, we now can use an arbitrary tomographic reconstruction method. We chose the additive ART method [39]. The initial reconstruction is set to null intensity
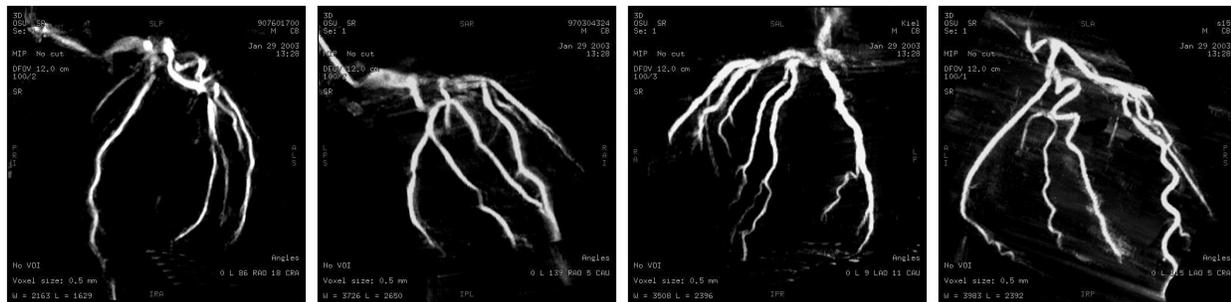
Fig. 7. MIP views of tomographic reconstructions (256^3, voxel size of 0.5 mm) of a panel of 4 patients.

for all voxels, then an iterative update is done pixel-wise by additive distribution of the projection residuals for a given pixel. More precisely, if $\mathbf{r}$ is a vector representing the current reconstruction, then the sum of contributions associated to pixel p_i in image n is given by $\mathbf{P}_i^\Phi \mathbf{r}$, where $\mathbf{P}_i^\Phi$ is the raw of matrix $\mathbf{P}^\Phi$ corresponding to pixel p_i contributions. The residual for pixel p_i is thus given by $J_n(p_i) - \mathbf{P}_i^\Phi \mathbf{r}$ and is homogeneously parted between contributing voxels by $\frac{J_n(p_i) - \mathbf{P}_i^\Phi \mathbf{r}}{\|\mathbf{P}_i^\Phi\|^2} \mathbf{P}_i^\Phi{}^T$, as sketched by the following update scheme:

$$\mathbf{r} \longleftarrow \mathbf{r} + \frac{J_n(p_i) - \mathbf{P}_i^\Phi \mathbf{r}}{\|\mathbf{P}_i^\Phi\|^2} \mathbf{P}_i^\Phi{}^T \qquad (19)$$

An iteration of ART algorithm is given by performing updates associated to all available pixels. In practice, we used 2 iterations of ART algorithm.

VI. EXPERIMENTS

A. Practical issues

There are a number of parameters in the proposed method: scales (section III-A), thresholds (section III-B.2 and Eq. (6)), weights (α in Eq. (7), α_1, α_2, and α_3 in Eq. (15)), etc. Since the aim of this study is to define and to assess a method that can be used in a clinical environment, manual parameter tuning is not desirable. Therefore, these parameters have been tuned experimentally on a subset of the patient datasets at hand, by visually inspecting intermediate and final results obtained by different values of parameters. The obtained settings have been retained for all the datasets, and the obtained automated method yields, after visual inspection, satisfactory results.

To reduce the computation time, both the 4-D motion estimation (section IV) and the tomographic reconstruction (section V) have been parallelized using PVM [40].

Typical computational times are (for a dataset consisting in 120 images at 512^2 spatial resolution, including 5 reference images): from 10 to 50 minutes for the reconstruction of a 3-D centerline model, from 15 to 30 minutes for the 4-D motion estimation, and about one hour for the tomographic reconstruction.

B. Reconstruction results

The reconstruction method was experimented on synthetical or phantom data, with a known 4-D motion. The obtained results, available in [12], [41], shown that, for such perfect

situations where the ground truth is known, the proposed method was able to retrieve the 4-D motion and to provide a good tomographic reconstruction.

The reconstruction of patient's data is more challenging, and is also more difficult to assess. We already exemplified the proposed approach with a number of results obtained with four different patient datasets, respectively used in Figures 4, and 6, Figure 5, and Figure 8. This illustrates the anatomical variability that can be successfully handled by the reconstruction method. In addition, Figure 7 depicts the Maximum Intensity Projection views of the reconstructions of 4 different patient datasets.

VII. DISCUSSION

We have described a tomographic reconstruction method from one single rotational acquisition and the results obtained so far demonstrate the feasibility of the proposed approach. The final as well as the intermediate results have the potential to support the image interpretation and quantification by the physician.

- Centerline reconstruction allows to estimate the magnification factor attached to a 2-D point (at a reference time) which yields better measurements, as well as optimal viewing angles to avoid overlap and vessel shortening [9], [42].
- 4-D motion estimation allows to track a point along the acquisition sequence. This enables a *stabilized display* of a region of interest, e.g. around a lesion (see Figure 8 and [43] for details). Moreover, by extrapolation it may give access to kinetic information about the myocardium.
- 3-D tomographic reconstruction allows to use standard 3-D visualization tools (isosurface, volume rendering, endoluminal views, etc.). It should be pointed out that, thanks to the 4-D motion estimation, renderings from arbitrary viewing angle and cardiac phase can be provided. More importantly, it allows a true 3-D QCA procedure, *i.e.* a quantitative 3-D measure of stenosis severity (cf Figure 9). Such a measure can be assessed with the catheter, whose diameter is 2.0 millimeters, when it is visible in the whole sequence [41]. In these cases, the measured mean diameter is about 2.3 millimeters. The error is then of the same order than the voxel size (0.25 millimeter). However, extrapolating this measure assessement to the
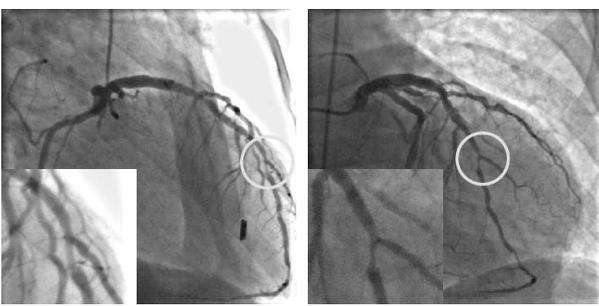
Fig. 8. Stabilized display of a stenosis. Two images that were acquired at distinct cardiac phases, from distinct viewing angles, in which we manually pointed the moving region of interest (a stenosis located at a bifurcation). Bottom left in images: focused and automatically centered images around the region of interest in the same images.
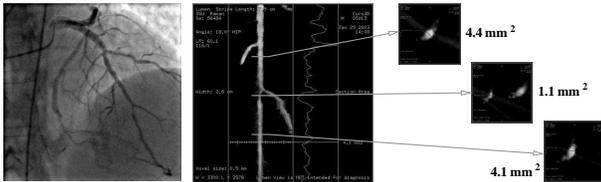

Fig. 9. Left: original angiogram. Right: vessel cross-sections measures (before, at, and after a stenosis).

coronary arteries is not straightforward, since the catheter may have a more simpler motion.

Obviously, such assertions have to be verified through clinical validation studies. Before initiating them, a retrospective analysis of our experiments is currently conducted.

The presented results and computation times have been obtained with the angiograph acquisitions being subsampled (from 768×768 to 512×512 pixels), for computational purposes. Additional experiments, conducted with full resolution images, did not show any visual difference.

At this point, we systematically use the end-diastole images as reference images to reconstruct a 3-D centerline model. In the future, it would be interesting to automatically select the most stable period of the cardiac cycle, which is the appropriate period for 3-D reconstruction, and that may depend on the heart rate.

We remark that the quality of the reconstruction (assessed visually) is directly correlated to the number of cardiac cycles that can be used for the processing. Typically, a number of 4 cardiac cycles (this corresponds to 5 reference times, *i.e.* $\tilde{\mathcal{R}} = 5$) yields a visually good reconstruction, while artifacts or errors (for instance, in the centerline reconstruction) are more likely to occur when only 3 cardiac cycles are usable. The latter situation mainly arises because of a poor synchronization between rotation and contrast agent injection. Such defects happened for the first acquisitions, when the physicians did not master the rotational acquisition, but not for the last ones because of a fast learning curve [13]. It suggests that the quality of the reconstructions will increase for the future experiments.

We observe that the computational time of the reconstruction of a 3-D centerline model represents about one third of the total execution time. This is due to the re-estimation of the

camera parameters, *i.e.* the respiratory motion (modeled as a translation) estimation. Since the acquisition duration is about a few seconds, it is possible to ask for a breath hold during the acquisition. This way, not only the total reconstruction time will be greatly decreased, but we will make sure to avoid the additional problems due to the respiratory motion estimation.

The roots of the coronary arteries are difficult to reconstruct since they are perpendicular to the rotation axis. This particular point is going to be investigated in relation with clinical partners.

It turns out that the first improvements will come from the design of an other acquisition protocol. Then, some quantitative quality measures have to be defined to assess both the overall quality of the reconstruction and all the different steps of the method (now excluding the respiratory motion estimation). This will help to optimize each step separately (*e.g.* the fusion of the centerline reconstructions). An other improvement in the future could be to automatically identify not only the heart cycles as we do now but also to identify the most appropriate period in the heart cycle for applying the multi-ocular algorithm. From the algorithm perspective, it has to be the most stable period along the heart cycle.

VIII. CONCLUSION

We presented a novel and stand-alone method to successively produce a 3-D reconstruction of coronary artery centerlines, a 4-D motion estimation of coronary arteries, and a 3-D tomographic reconstruction of coronary arteries from one single rotational X-ray acquisition. In contrast to other approaches reported in the literature, we are able to use almost all of the acquired frames, thank to the estimation of the coronary arteries motion.

Experiments conducted on real clinical data produced visually good reconstructions which demonstrate the practicability of such an approach. A further analysis encourages us to define a different acquisition protocol (with a breath hold) to suppress artifacts due to the respiratory estimation. Future work will consist of a clinical evaluation of the method, and will encompass both a quantitative assessment of the quality of the reconstruction and the identification of methodological improvements.

REFERENCES

[1] J. Mackay and G. A. Mensah, Eds., *The Atlas of Heart Disease and Stroke*. World Health Organization, 2004. [Online]. Available: http://www.who.int/cardiovascular_diseases/resources/atlas/en/

[2] S. Ruan, A. Bruno, and J. Coatrieux, "3D motion and reconstruction of coronary arteries from biplane cineangiography," *Image and Vision Computing*, vol. 12, no. 10, pp. 683–689, 1994.

[3] A. Wahle, H. Oswald, and E. Fleck, "3D heart-vessel reconstruction from biplane angiograms," *IEEE Computer Graphics and Applications*, vol. 16, no. 1, pp. 65–73, 1996.

[4] S. Y. Chen and C. E. Metz, "Improved determination of biplane imaging geometry from two projection images and its application to three-dimensional reconstruction of coronary arterial trees," *Med Phys*, vol. 24, no. 5, pp. 633–54, 1997.

[5] S. J. Chen and J. D. Carroll, "3-d reconstruction of coronary arterial tree to optimize angiographic visualization," *IEEE Trans Med Imaging*, vol. 19, no. 4, pp. 318–36, 2000.

[6] S. Raman, R. Magorien, R. Vaillant, P. Payne, K. Benali, and C. Bush, "Rotational Cardiovascular X-Ray Imaging for Left Coronary Artery Angiography Using a Digital Flat-Panel Cardiac Imaging System," *American Journal of Cardiology*, vol. 90, no. 6A, 2002.

[7] E. Kuon, P. Niederst, and J. Dahm, "Usefulness of Rotational Spin for Coronary Angiography in Patients with Advanced Renal Insufficiency," *American Journal of Cardiology*, vol. 90, no. 4, pp. 369–373, 2002.

[8] V. Rasche, M. Grass, R. Koppe, A. Bücker, R. Günther, H. Kühl, J. Op de Beek, R. Bertrams, and R. Suurmond, "ECG-gated 3D rotational coronary angiography," in *Proceedings of Computer Assisted Radiology and Surgery*. Paris: Springer-Verlag, 2002, pp. 826–831.

[9] O. Wink, R. Kemkers, S.-Y. J. Chen, S. Chen, and J. D. Carroll, "Intra-procedural coronary intervention planning using hybrid 3-dimensional reconstruction techniques," *Academic Radiology*, vol. 10, no. 12, pp. 1433–41, 2003.

[10] B. Movassaghi, V. Rasche, M. Grass, M. A. Viergever, and W. J. Niessen, "A quantitative analysis of 3-d coronary modeling from two or more projection images," *IEEE Trans Med Imaging*, vol. 23, no. 12, pp. 1517–31, 2004.

[11] S. Bonnet, A. Koenig, S. Roux, P. Hugonnard, R. Guillemaud, and P. Grangeat, "Dynamic X-ray computed tomography," *Proceedings of the IEEE*, vol. 91, no. 10, pp. 1574–1587, 2003, emerging Medical Imaging Technology.

[12] C. Blondel, R. Vaillant, G. Malandain, and N. Ayache, "3D tomographic reconstruction of coronary arteries using a precomputed 4D motion field," *Physics in Medicine and Biology*, vol. 49, no. 11, pp. 2197–2208, 2004, special Issue: Seventh International Meeting on Fully 3D Image Reconstruction in Radiology and Nuclear Medicine.

[13] S. V. Raman, R. Morford, M. Neff, T. T. Attar, G. Kukielka, R. D. Magorien, and C. A. Bush, "Rotational X-ray coronary angiography," *Catheterization and Cardiovascular Interventions*, vol. 63, no. 2, pp. 201–7, 2004.

[14] J. Serra, *Image analysis and mathematical morphology*. Academic Press, 1982.

[15] A. Frangi, W. Niessen, K. Vincken, and M. Viergever, "Multiscale Vessel Enhancement Filtering," in *Proceedings of Medical Image Computing & Computer Assisted Intervention (MICCAI) 1998*, ser. LNCS, W. Wells, A. Colchester, and S. Delp, Eds., vol. 1496. Springer-Verlag, 1998, pp. 130–137.

[16] Y. Sato, S. Nakajima, N. Shiraga, H. Atsumi, S. Toshida, T. Koller, G. Gerig, and R. Kikinis, "3D multi-scale line filter for segmentation and vizualisation of curvilinear structures in medical images," *Medical Image Analysis*, vol. 2, no. 2, pp. 143–168, 1998.

[17] K. Krissian, G. Malandain, N. Ayache, R. Vaillant, and Y. Trousset, "Model-based detection of tubular structures in 3D images," *Computer Vision and Image Understanding*, vol. 80, no. 2, pp. 130–171, 2000.

[18] C. Lorenz, I. Carlsen, T. Buzug, C. Fassnacht, and J. Weese, "Multi-scale line segmentation with automatic estimation of width, contrast and tangential direction in 2D and 3D medical images," in *Proceedings of CVRMed-MRCAS*, ser. LNCS, J. Troccaz, W. Grimson, and R. Mösges, Eds., vol. 1205. Grenoble: Springer-Verlag, 1997, pp. 233–242.

[19] T. Lindeberg, *Scale-Space Theory in Computer Vision*. Dordrecht, Netherlands: Kluwer Academic Publishers, 1994.

[20] G. Giraudon, "An Efficient Edge Following Algorithm," in *Proceedings of 5th Scandinavian Conference on Image Analysis*, vol. 2, Stockholm, 1987, pp. 547–554.

[21] A. Merle, G. Finet, J. Liénard, and I. Magnin, "3D reconstruction of deformable coronary tree skeleton from two X-ray angiographic views," in *Proceedings of Computers in Cardiology*. Cleveland, Ohio: IEEE, 1998, pp. 775–760.

[22] C. Blondel, R. Vaillant, F. Devernay, G. Malandain, and N. Ayache, "Automatic Trinocular 3D Reconstruction of Coronary Artery Center-lines from Rotational X-ray Angiography," in *Proceedings of Computer Assisted Radiology and Surgery (CARS)*. Paris: Springer-Verlag, 2002, pp. 832–837.

[23] E. Dijkstra, "A note on two problems in connection with graphs," *Numerische Mathematik*, vol. 1, pp. 269–271, 1959.

[24] Y. Wang, S. Riedere, and R. Ehman, "Repiratory Motion of the Heart: Kinematics and the Implications for the spatial resolution in coronary imaging," *Magnetic Resonance in Medicine*, vol. 33, no. 5, pp. 713–719, 1995.

[25] A. Holland, J. Goldfarb, and R. Edelman, "Diaphragmatic and cardiac motion during suspended breathing: Preliminary experience and implications for breath-hold MR imaging," *Radiology*, vol. 209, no. 2, pp. 483–489, 1998.

[26] P. Danias, M. Stuber, R. Botnar, K. Kissinger, R. Edelman, and W. Manning, "Relationship between motion of coronary arteries and diaphragm during free breathing: Lessons from real-time MR imaging," *American Journal of Roentgenology*, vol. 172, no. 4, pp. 1061–1065, 1999.

[27] J. Keegan, P. Gatehouse, G. Yang, and D. Firmin, "Coronary artery motion with the respiratory cycle during breath-holding and free-breathing: implications for slice-followed coronary artery imaging," *Magnetic Resonance in Medicine*, vol. 47, no. 3, pp. 476–481, 2002.

[28] C. Blondel, G. Malandain, R. Vaillant, F. Devernay, E. Coste-Manière, and N. Ayache, "4D Tomographic Representation of Coronary Arteries From One Rotational X-Ray Sequence," in *Proceedings of Medical Image Computing & Computer Assisted Intervention (MICCAI)*, ser. LNCS, vol. 2878. Montreal: Springer-Verlag, 2003, pp. 416–423.

[29] C. Lawrence, J. Zhou, and A. Tits, *User's Guide for CFSQP Version 2.5: A C Code for Solving (Large Scale) Constrained Nonlinear (Minimax) Optimization Problems, Generating Iterates Satisfying All Inequality Constraints*, University of Maryland, 1997. [Online]. Available: http://www.aemdesign.com/download-cfsqp/cfsqp-manual.pdf

[30] C. Lawrence and A. Tits, "A Computationally Efficient Feasible Sequential Quadratic Programming Algorithm," *SIAM Journal on Optimization*, vol. 11, no. 4, pp. 1092–1118, 2001.

[31] G. Shechter, F. Devernay, A. Quyyumi, E. Coste-Manière, and E. McVeigh, "Three-Dimensional Motion Tracking of Coronary Arteries in Biplane Cineangiograms," *IEEE Transactions in Medical Imaging*, vol. 22, no. 4, pp. 493–603, 2003.

[32] S. Y. J. Chen, S. Chen, and J. D. Carroll, "Kinematic and deformation analysis of 4-d coronary arterial trees reconstructed from cine angiograms," *IEEE Trans Med Imaging*, vol. 22, no. 6, pp. 710–21, 2003.

[33] M. Unser, "Splines: A perfect fit for signal and image processing," *IEEE Signal Processing Magazine*, vol. 16, no. 6, pp. 22–38, 1999, IEEE Signal Processing Society's 2000 Magazine Award. [Online]. Available: http://bigwww.epflch/publications/unser9902.html

[34] P. Radeva, A. Amini, and J. Huang, "Deformable B-solids and implicit snakes for 3D localization and tracking of SPAMM MRI data," *Computer Vision and Image Understanding*, vol. 66, no. 2, pp. 163–178, 1997.

[35] P. Gill, W. Murray, and M. Wright, *Practical optimization*. Academic Press, 1982.

[36] G. Vanderplaats, *CONMIN - A ForTran program for constrained function minimization - User's manual*, NASA, 1978, technical Memorandum X-62282. [Online]. Available: http://mdob.larc.nasa.gov/mdo.test/CONMIN/manual.html

[37] J. Hsieh, E. Chao, J. Thibault, B. Grekowicz, A. Horst, S. McOlash, and T. J. Myers, "A novel reconstruction algorithm to extend the ct scan field-of-view," *Med Phys*, vol. 31, no. 9, pp. 2385–91, 2004.

[38] B. Movassaghi and V. Rasche, "3D coronary reconstruction from calibrated motion-compensated 2D projections based on semi-automated feature point detection," in *Proceedings of SPIE Medical Imaging: Image Processing*, Newport Beach, CA, 2004.

[39] G. Herman, *Image reconstruction from projections*. Academic Press, 1980.

[40] A. Geist, A. Beguelin, J. Dongarra, W. Jiang, R. Manchek, and V. Sunderam, "PVM 3 user's guide and reference manual," Oak Ridge National Laboratory, Tech. Rep. ORNL/TM-12187, 1993.

[41] C. Blondel, G. Malandain, R. Vaillant, and N. Ayache, "Reconstruction of coronary arteries from one rotational X-ray projection sequence," INRIA, Research report 5214, 2004. [Online]. Available: http://www.inria.fr/rrrt/rr-5214.html

[42] T. Sato, T. Araki, and M. Hanayama, "A viewpoint determination system for stenosis diagnosis and quantification in coronary angiographic image acquisition," *IEEE Transactions on Medical Imaging*, vol. 17, no. 1, pp. 121–137, 1998.

[43] C. Blondel, G. Malandain, R. Vaillant, and N. Ayache, "4D Deformation Field of Coronary Arteries from Monoplane Rotational X-Ray Angiography," in *Proceedings of Computer Assisted Radiology and Surgery (CARS)*, ser. International Congress Series, vol. 1256. London: Elsevier, 2003, pp. 1073–1078.